

Imaging the South Pole - Aitken Basin in Backscattered Neutral Hydrogen Atoms

A. Vorburger^{a,*}, P. Wurz^b, S. Barabash^c, M. Wieser^c, Y. Futaana^c,
A. Bhardwaj^d, K. Asamura^e,

^a*Division of Physical Sciences, American Museum of Natural History, New York, USA*

^b*Physikalisches Institut, Universität Bern, Sidlerstrasse 5, CH-3012 Bern, Switzerland*

^c*Swedish Institute of Space Physics, Box 812, SE-98128 Kiruna, Sweden*

^d*Space Physics Laboratory, Vikram Sarabhai Space Center, Trivandrum 695 022, India.*

^e*Institute of Space and Astronautical Science, 3-1-1 Yoshinodai, Sagami-hara, Japan.*

Abstract

The lunar surface is very efficient in reflecting impinging solar wind ions as energetic neutral atoms (ENAs). A global analysis of lunar hydrogen ENAs showed that on average 16% of the solar wind protons are reflected, and that the reflected fraction can range from less than 8% to more than 24%, depending on location. It is established that magnetic anomalies reduce the flux of backscattered hydrogen ENAs by screening-off a fraction of the impinging solar wind. The effects of the surface properties such as porosity, roughness, chemical composition, and extent of weathering, was not known.

In this paper, we conduct an in-depth analysis of ENA observations of

*Corresponding author

Email: avorburger@amnh.org

Telephone: +1 212 796 5082

the South Pole - Aitken basin to determine which of the surface properties might be responsible for the observed variation in the integral ENA flux. The South Pole - Aitken basin with its highly variable surface properties is an ideal object for such studies. It is very deep, possesses strikingly elevated concentrations in iron and thorium, has a low albedo and coincides with a cluster of strong magnetic anomalies located on the northern rim of the basin. Our analysis shows that whereas, as expected, the magnetic anomalies can account well for the observed ENA depletion at the South Pole - Aitken basin, none of the other surface properties seem to influence the ENA reflection efficiency. Therefore, the integral flux of backscattered hydrogen ENAs is mainly determined by the impinging plasma flux and ENA imaging of backscattered hydrogen captures the electrodynamics of the plasma at the surface. We cannot exclude minor effects by surface features.

Keywords: Moon, South Pole - Aitken Basin, Energetic Neutral Atoms, Backscattering

1. Introduction

The Moon, not being protected by a global magnetic field nor by an atmosphere, is constantly bombarded by solar wind ions. Until a few years ago, it was commonly assumed that the impinging solar wind ions are almost

5 completely absorbed by the lunar surface (e.g. Crider and Vondrak (2002);
6 Feldman et al. (2000)). This assumption has been invalidated by several
7 recent observations conducted by Nozomi (Futaana et al., 2003), Kaguya
8 (Saito et al., 2008), Chandrayaan-1 (Wieser et al., 2009; Lue et al., 2011), the
9 Interstellar Boundary Explorer (IBEX) (McComas et al., 2009), Chang'E-1
10 (Wang et al., 2010) and Artemis (Halekas et al., 2013).

11 In particular, observations by Kaguya and Chandrayaan-1 showed that
12 in fact on average between 0.1% and 1% of the impinging solar wind ions
13 are reflected back from the lunar surface as ions, with local values ranging
14 from 0% to more than 50% (Saito et al., 2008; Lue et al., 2011). Moreover,
15 IBEX and Chandrayaan-1 observations showed that on average 16% of the
16 impinging solar wind protons are backscattered as neutral hydrogen atoms
17 from the lunar surface (McComas et al., 2009; Wieser et al., 2009; Vorburger
18 et al., 2013). Mapping of the complete Chandrayaan-1 dataset showed that
19 this backscatter percentage can range from less than 8% to more than 24%
20 (Vorburger et al., 2013).

21 While an in-depth analysis of several observations of local magnetic anoma-
22 lies showed that these could influence the amount of solar wind flux reaching
23 the lunar surface (e.g. Lin et al. (1998); Wieser et al. (2010); Saito et al.

24 (2010); Lue et al. (2011); Vorburger et al. (2012)), influences of other surface
25 properties on the ion - surface interaction have not been investigated. We
26 thus chose to analyze the ENA measurements in a region that exhibits very
27 distinct features in as many surface properties as possible.

28 With the South Pole - Aitken basin exhibiting distinct variability of
29 several properties potentially affecting the ion - surface interaction (visible
30 albedo, topography, chemistry, mineralogy, magnetism), it poses a choice lo-
31 cation for analyzing the interaction between the solar wind and the lunar
32 surface. By comparing an ENA integral flux map to variations in the differ-
33 ent maps, we can determine what surface properties ENAs are sensitive to.
34 This helps us shed more light onto the still poorly understood backscattering
35 process of plasma ions from regolith covered planetary surfaces.

36 The role of crustal magnetic fields on the lunar surface for the observa-
37 tion of these ENAs is that the plasma physical interaction of the solar wind
38 plasma with the surface magnetic fields governs actual access of ions to the
39 surface, as has been demonstrated in several papers before (Vorburger et al.,
40 2012, 2013). Scattering of atoms and ions at solid surfaces is a complex pro-
41 cess where the interaction of the impinging particles with the surface atoms
42 is determined by the top-most surface of the solid, its chemical composition,

43 and its roughness (Niehus et al., 1993). Variations in visible albedo of the
44 Moon can have several causes, for example an increased roughness of the
45 surface at scales commensurate with optical wavelengths can cause a lower
46 visible albedo or a different chemical (or mineralogical) composition. Both of
47 these effects will cause differences in the particle scattering from the surfaces:
48 increased roughness will reduce the efficiency of particle reflection to space
49 because of multiple scattering at the fractal surfaces and higher probability
50 of absorption of a particle, and a different chemical composition changes the
51 scattering partners for the reflection since this interaction is to first order a
52 single or a few binary collisions. The South-pole Aitken basin is the oldest
53 recognized topographical feature on the lunar surface. With its size of about
54 2500 km and a depth of about 12 km it indicates that a substantial amount of
55 material has been removed from the surface during the impact forming this
56 basin. Thus, the material on the floor of this basin might be different from
57 the material outside this basin. The chemical and mineralogical composition
58 of the South-pole Aitken basin is different from typical highland regions, as
59 as recorded in data from the Galileo, Clementine and Lunar Prospector mis-
60 sions (e.g. Lawrence et al. (1998, 2002)), thus possibly affecting the ENA
61 albedo. In terms of mineralogy, the basin floor is much richer in clinopyrox-

ene (monoclinic crystal) and orthopyroxene (orthorhombic crystals) minerals than the surrounding highlands that are largely anorthositic (mostly plagioclase feldspar with minor mafic contributions). Pyroxenes are Si- or Al-oxide based minerals with ions of Ca, Na, Mg, Fe and other elements, many of heavier mass than in the anorthositic highlands, again, which might affect the ENA albedo. The remote sensing observations indicate that the floor of this basin has slightly elevated abundances of iron, titanium, and thorium. The enrichment in several heavier elements, which may represent lower crust material, will affect the particle.

In Chapter 1 we briefly describe the instrument and the observations that were used for this analysis. In Chapter 2 we discuss the different surface features in which the South Pole - Aitken basin is distinguished from the surrounding terrain, and present two maps showing the ENA observations of that region. In Chapter 3 we thoroughly discuss the correlation between the ENA map and local surface features and the thus deduced implications as to what mechanisms can cause the observed ENA depletions. Chapter 4 presents our conclusions and discusses where else our results might be applicable.

80 2. Observations and Instrumentation

81 For this study we analyzed measurements conducted by the Chandrayaan-
82 1 Energetic Neutrals Analyzer (CENA) (Kazama et al., 2007), which is a part
83 of the Sub-keV Atom Reflecting Analyzer (SARA) instrument (Bhardwaj
84 et al., 2005; Barabash et al., 2009) on board Chandrayaan-1 (Goswami and
85 Annadurai, 2009). CENA measured ENAs originating from the lunar surface
86 within the energy range 10 eV to 3.3 keV and with an energy resolution of
87 $\Delta E/E \approx 50\%$. Even though CENA allows crude mass analysis to identify
88 H, He, and O (Vorburger et al., 2014), we only analyzed hydrogen measure-
89 ments in this study because the hydrogen counts by far exceed the counts
90 in all other mass bins combined, thus they offer the statistically most robust
91 measurement by far. CENA’s field-of-view is spanned by seven angular sec-
92 tors, which provide information about the arrival direction of the measured
93 ENAs. The central sector is nadir pointing, i.e., its bore-sight crosses the
94 lunar surface at the sub-spacecraft point. The other six sectors are symmet-
95 rically arranged around the central sector in the azimuth direction covering
96 a swath of the full size of the Moon perpendicular to the orbit motion (see
97 Figure 1 in Wieser et al. (2010) for an illustration). Measurements by the
98 outermost two sectors were disregarded in this study because they not only

99 record measurements from the lunar surface but also from the lunar limb.
 100 The surface projections of the remaining five sectors are given in Table 1.
 101 The Chandrayaan-1 mission operated from October 2008 until the end
 102 of August 2009. The spacecraft's circular polar orbit was initially set at
 103 an altitude of 100 km and was raised to 200 km at the end of May 2009.
 104 Discarding the period when the Moon was inside Earth's magnetosphere,
 105 we were left with 163 orbits, 64 of which passed directly over the South
 106 Pole - Aitken basin (i.e. the instrument's boresight crossed the South Pole
 107 - Aitken basin). Since each orbit gives us 5 datasets (one for each angular
 108 sector), we had in total 815 datasets to analyze, about 250 of which contained
 109 measurements from the South Pole - Aitken basin.

110 **3. The South Pole - Aitken Basin**

111 *3.1. The South Pole - Aitken Basin in ENAs*

112 Figure 1 shows two different ENA reflection ratio maps centered on the
 113 South Pole - Aitken basin. The reflection ratio is defined as the ratio of ENA
 114 flux backscattered from the lunar surface for CENA's complete energy range

115 and all exit angles (hemisphere) to the impinging solar wind ions:

$$116 \quad R = \frac{J_{\text{ENA}}}{J_{\text{SW}}}, \quad (1)$$

117 where J_{ENA} is the reflected ENA flux over the zenith hemisphere (the 2π
 118 sphere) and J_{SW} is the impinging solar wind flux observed at the Moon.
 119 The solar wind values were taken from the WIND spacecraft time-shifted
 120 according to the distance between WIND and Chandrayaan-1 as well as the
 121 plasma's velocity.

122 Since a single ENA observation is only able to measure the flux backscat-
 123 tered in a certain direction (i.e., towards the instrument's field of view), we
 124 first had to deduce the total ENA flux released over the complete zenith hemi-
 125 sphere (J_{ENA}) from the directional measurement ($j_{\text{ENA}}(\text{SZA}, \phi, \theta)$). This was
 126 accomplished by fitting the measurements with the scattering function pre-
 127 sented in Appendix A in Vorburger et al. (2013), which gives for every angle
 128 of incidence of the solar wind ions the angular distribution of the backscat-
 129 tered ENA flux. Equation 1 thus becomes:

$$130 \quad R = \frac{j_{\text{ENA}}(\text{SZA}, \phi, \theta)}{J_{\text{SW}} \cdot f_S(\text{SZA}, \phi, \theta)}, \quad (2)$$

131 where $j_{\text{ENA}}(\text{SZA}, \phi, \theta)$ is the directional ENA flux, and where $f_S(\text{SZA}, \phi, \theta)$
 132 is the directional scattering function. To compensate for the intrinsically low
 133 number of counts towards the poles, we applied the same flat-field correction
 134 as described in Vorburger et al. (2012). Once we computed the reflection
 135 ratio for each individual measurement, we combined all measurements into
 136 a single map. We decided to divide the map up into two energy ranges
 137 to see if variations present in the ENA maps depend on the energy of the
 138 reflected atoms with respect to the impacting protons. Figure 1 panel a)
 139 shows the lower half of the energy range (ENAs with energies $< 30\%$ of the
 140 energy of the currently impinging solar wind plasma) and panel b) shows the
 141 upper half of the energy range (ENAs with energies $> 30\%$ of the energy
 142 of the currently impinging solar wind plasma). The red polygons in both
 143 panels denote the approximate extension of the ENA feature. In addition,
 144 we over-plotted the topographic structure of the South Pole - Aitken basin
 145 in white (see text below). Figure 1 panel c) shows the effective exposure
 146 time for each point on the surface. To correct for the non-uniform angular
 147 response of each sector, the total exposure time of 4 s of each measurement
 148 was multiplied with a two-dimensional Gaussian distribution covering the
 149 given sector's surface projected field of view. The effective exposure time in

150 Figure 1 panel c) is the sum of all of these fractions. When plotting the data,
151 to ensure that the statistics are sufficient, we required a minimal exposure
152 time of 1 sec. In addition, due to the steep decrease in counting statistics
153 towards the polar regions, we cut off data below -70° and above 70° latitude.
154 Figure 1 panel d) shows for comparison the magnetic field magnitude at
155 30 km altitude as measured by Lunar Prospector.

156 *3.2. The South Pole - Aitken Basin in other features*

157 The South Pole - Aitken basin is the most pronounced topographic struc-
158 ture on the Moon. The highly-degraded appearance and large number of
159 superimposed craters suggest that it may be the oldest basin on the Moon.
160 It is located at (180°E , 56°S), has a diameter of ~ 2500 km, and is ~ 12 km
161 deep (McFadden et al., 2007). Topography and gravity measurements imply
162 that whereas the lunar crust has an average thickness of about 50 km, the
163 crust is reduced to a thickness of about 15 km within the basin (Wieczorek
164 et al.). A global albedo map from the 750-nanometer filter of the Clementine
165 UV-VIS camera shows that the South Pole - Aitken basin is also distin-
166 guishable by eye as a dark mafic anomaly (Lee et al., 2009). In addition,
167 the South Pole - Aitken basin differs compositionally from the surrounding
168 highland terrain. Lunar Prospector gamma-ray and neutron spectrometer

169 measurements showed that FeO abundances are highly elevated in the South
170 Pole - Aitken basin and almost reach levels measured in the nearside maria
171 (Lawrence et al., 2002). Other examples for compositional differences apply
172 to thorium, potassium, titanium, magnesium, uranium, and samarium, the
173 abundances of which are low compared to the abundances found in the near-
174 side maria, but which are distinctly elevated in the South Pole - Aitken basin
175 compared to the surrounding highland terrain (Lawrence et al. (1998); Zhang
176 and Bowles (2013), and available Lunar Prospector Spectrometer data).

177 Garrick-Bethell and Zuber (2009) analyzed the structure of the South
178 Pole - Aitken basin based on topography, iron, thorium, albedo and spec-
179 tral band ratio maps. They showed that the shapes of the boundaries of
180 the low topography and elevated iron and thorium content regions are well
181 described by elliptical shapes that are oriented along the same azimuth,
182 have nearby centers, similar eccentricities, and centers that lie along their
183 common azimuth. In addition, they showed that the albedo and spec-
184 tral band ratio structures fit well within the topography elliptical shape.
185 Figure 2 displays four of the five maps used in the analysis by Garrick-
186 Bethell and Zuber (2009). Panel a) displays Clementine laser altimeter
187 data, mapped at 0.25 pixel per degree resolution. The Clementine laser

188 altimeter data was acquired from ([http://pds-geosciences.wustl.edu/](http://pds-geosciences.wustl.edu/missions/clementine/gravtopo.html)
189 [missions/clementine/gravtopo.html](http://pds-geosciences.wustl.edu/missions/clementine/gravtopo.html)). Panels b) and c) display Lunar
190 Prospector gamma-ray spectrometer iron and thorium data, mapped at 0.5
191 pixel per degree resolution. The Lunar Prospector gamma-ray spectrometer
192 data were obtained from ([http://pdsgeosciences.wustl.edu/missions/](http://pdsgeosciences.wustl.edu/missions/lunarp/reduced_special.html)
193 [lunarp/reduced_special.html](http://pdsgeosciences.wustl.edu/missions/lunarp/reduced_special.html)). Panel d) displays a global Clementine
194 750 nm spectral reflectance mosaic which was downloaded from ([http://](http://astrogeology.usgs.gov)
195 astrogeology.usgs.gov).

196 The South Pole - Aitken basin can, in addition, be easily identified in
197 magnetic field maps, where large clusters of magnetic fields coincide with the
198 northern rim of the basin (e.g. Purucker et al. (2006); Richmond and Hood
199 (2008); Mitchell et al. (2008); Hood et al. (2013)). The origin of these mag-
200 netic fields is still under debate. Two currently dominating hypotheses pro-
201 pose quite the opposite: While one proposes that an impact antipodal of the
202 South Pole - Aitken basin is responsible for the magnetic anomalies related
203 to the South Pole - Aitken basin (e.g. Hood et al. (2013)), the other proposes
204 that the impact creating the South Pole - Aitken basin itself is associated
205 with the observed magnetic anomalies (e.g. Wieczorek et al.). We show the
206 magnetic field magnitude at 30 km altitude as measured by Lunar Prospec-

207 tor in Figure 2 panel e). The Lunar Prospector data were obtained from
208 (<http://pds-geosciences.wustl.edu/missions/lunarp/mager.html>).

209 For comparison, we over-plotted in panels a) through e) the ellipse fitting
210 the topography data best in white, the respective ellipses fitting the iron
211 and thorium data best in yellow, and the polygon denoting the approximate
212 extension of the ENA feature in red.

213 4. Discussion

214 We compare our ENA maps to the individual maps shown in Figure 2 for
215 the South Pole Aitken basin area. The topography structure of the South
216 Pole - Aitken basin seems well constrained by the ellipse depicted in Fig-
217 ure 2 panel a). The elevation within this ellipse appears roughly constant,
218 with slightly lower altitudes in the south-eastern part of the South Pole -
219 Aitken basin. The low- and the high-energy ENA maps show reflection ratio
220 reductions that are mostly confined to the north-western and central parts
221 of the ellipse (areas 2 and 5, Figure 2 panel f), and extend beyond the basin
222 (i.e., the ellipse) northwards to a large part (area 1). Furthermore, while
223 the eastern part of the reduced reflection ratio region is confined to longi-
224 tudes smaller than -150° , the ellipse reaches -120° in longitude. In addition,

225 north-east of the South Pole - Aitken basin, the elevation map exhibits high
226 mountain ranges. The ENA maps show no variation whatsoever in this area.

227 The areas of iron and thorium abundance enrichments share many char-
228 acteristics in their selenographic distribution. The centers for the ellipses are
229 almost on top of each other, they differ only by 4.2° in longitude and 2.8°
230 in latitude and the difference in tilt angle is 2.9° . Figure 2 shows these fits
231 together with the ellipse from topography. The most striking difference be-
232 tween the iron and thorium map is that the iron enrichment with respect to
233 the surrounding terrain is much more distinct: it is in fact more than twice
234 as intense as the thorium enrichment. Both iron and thorium exhibit high
235 abundances confined to the northern halves of the basin (see elemental abun-
236 dance ellipses in Figure 2). Their eastern confinement seems to agree better
237 with the ENA feature than the eastern confinement of the topography fea-
238 ture. Again, though, the low-ENA region extends far beyond the elemental
239 abundance regions towards the North.

240 The visible albedo map exhibits a high correlation with the topography
241 map, but it is not as well defined by the best fit topography ellipse (see Fig-
242 ure 2 panel d). Especially towards the southern pole, well within the ellipse,
243 the visible albedo increases rather abruptly. This north-south contrast is the

244 only agreement between the visible albedo and the ENA maps, though. Sim-
245 ilarly to the topography structure, the low-albedo region is very pronounced
246 in the eastern region of the ellipse, where no corresponding ENA feature can
247 be discerned.

248 The magnetic field measurements in general correlate much better with
249 the two ENA maps than the other previously discussed features. Both the
250 high magnetic field region and the low ENA region cluster around the north-
251 ern rim of the basin (areas 1 and 2) and are limited to smaller longitudes.
252 In addition, similar to the ENA feature, the magnetic field feature can not
253 be fitted as well with an ellipse as the other features, but exhibits a more
254 frayed structure. Two regions where the ENA maps and the magnetic field
255 map do not quite agree are the two magnetic anomalies just north of the
256 equator. These two anomalies are very small in extent, though, which could
257 either mean that they are too small to pose an obstacle to the impinging solar
258 wind ions, or that they cannot be resolved with CENA's angular resolution.
259 In addition, they were never directly in CENA's bore-sight, i.e., the counts
260 in these regions are always part of the Gaussian tail distribution over the
261 instrument's field of view (compare Figure 1 panel c). This could lead to the
262 anomalies being 'washed out' during the mapping process. Overall, the ENA

263 features in either energy range follow quite well variations in the magnetic
264 field strength at 30 km altitude.

265 In contrast to the Gerasimovich magnetic anomaly (located at $\sim -122^\circ$ longitude/-
266 22° latitude, having a diameter of ~ 26 km), where the magnetic anomaly is
267 well pronounced in the high energy map but is not visible in the low en-
268 ergy map (Wieser et al., 2009), we see that the South Pole - Aitken basin
269 is well pronounced in both energy ranges (Figure 1 panels a) and b). The
270 cause for the energy dependence at the Gerasimovich anomaly lies in the
271 dependence of the backscattered ENA spectrum on the impinging particle
272 velocity. Futaana et al. (2013) showed that the backscattered ENAs exhibit
273 a Maxwellian energy spectrum with the characteristic energy of ($k_B T = 60$
274 $- 160$ eV), which is linearly proportional to the impinging particle veloc-
275 ity. When the solar wind plasma interacts with a weak magnetic field of
276 an anomaly, the protons are decelerated by ambipolar electric field result-
277 ing from charge separation of magnetized electrons and non-magnetized ions.
278 The protons reach the surface with lower velocities and result in a spectrum
279 of backscattered ENAs with a lower temperature. The high energy range
280 thus becomes less populated and the respective reflection rate lower. The
281 magnetic anomaly located at the South Pole - Aitken basin is much larger

282 than the Gerasimovich anomaly (and in fact all other anomalies found on the
 283 lunar surface), though: The size of most magnetic anomalies is comparable
 284 to the proton gyro radius (Vorbürger et al., 2012), whereas the South Pole
 285 - Aitken basin spans over an area of about 10 proton gyro radii. The large
 286 size could be the reason for the similarity of the low and the high energy
 287 ENA maps at the South Pole - Aitken basin, because it allows for magnetic
 288 deflection also of decelerated ions at low energy. In addition, the highest
 289 fluxes of reflected solar wind ions were observed also in this area (Lue et al.,
 290 2011).

291 A summary of the different surface features for the five different regions
 292 denoted in Figure 2 panel f) is given in Table 2, where the numbers corre-
 293 spond to the averages of the respective features within each region. This
 294 table shows that the elevation and the visible albedo as well as the iron and
 295 the thorium map strongly agree, whereas the magnetic field map and the
 296 ENA maps strongly disagree in the analyzed five regions. We also computed
 297 the linear Pearson correlation coefficient between the two ENA maps and the
 298 other maps based on the values presented in Table 2. The coefficients are
 299 presented in Table 3. As one can see, the ENA maps strongly anti-correlate
 300 with the magnetic field maps. The only pair with a significant correlation

301 (p-value < 0.05) is the high energy ENA map and the magnetic field map.
302 The low energy ENA map shows a p-value slightly above the significance
303 threshold (p-value = 0.07).

304 Whereas it is difficult to completely rule out causes correlating with the
305 reflection of ENAs from the surface, the considerations above indicate that
306 whereas ENA fluxes are clearly sensitive to magnetic fields located on the
307 lunar surface, they are far less if not non- sensitive to changes in elevation,
308 chemical composition, and visible albedo. Since the ENAs are born from a
309 reflection of a proton on the very surface, i.e., by proton scattering from the
310 atoms on the surface of regolith grains, one would expect that changing the
311 chemical composition of the surface (c.f. iron and thorium maps) should alter
312 the scattering processes. Similarly, the visible albedo is a result of properties
313 of the very surface, e.g. the porosity, surface roughness, chemical composition
314 and others, thus it could have a correlation with the ENA fluxes. The deep
315 basin (elevation map) is the result of a major impact and thus younger than
316 the surrounding lunar high land terrain, less cratered also at very small scales,
317 and the regolith possibly less processed, which could affect the scattering
318 properties of solar wind ions. In all these cases, but the magnetic field, we
319 did not observe a clear correlation, though.

320 5. Conclusion

321 We compared our ENA measurements of the South Pole - Aitken basin to
322 topography, albedo, elemental composition and magnetic field measurements
323 of the basin. The comparison shows that whereas the ENAs are sensitive to
324 crustal magnetic fields, they are by far not as sensitive to elevation, visible
325 albedo, and the iron and thorium content. This suggests that the solar wind
326 - lunar surface interaction as observed via ENAs is the same everywhere on
327 the lunar surface irrespective of visible albedo, composition, elevation and
328 that the variation in ENA fluxes is a result of the magnetic fields present on
329 the surface. The indetermination of flux of backscattered hydrogen ENAs
330 is determined mainly by the impinging plasma flux and ENA imaging of
331 backscattered hydrogen captures the electrodynamics of the plasma at the
332 surface.

333 The analysis presented in this paper concerns only the total ENA flux.
334 Therefore, we cannot rule out weak dependences of the shape of backscattered
335 ENA spectra and/or scattering function on the surface properties. Studies
336 of such dependences would require ENA instruments with higher energy and
337 angular resolutions than CENA and different observation geometries from
338 the ones provided.

339 Detailed ENA measurements to study the interaction of solar wind plasma
340 and Mercury's surface are planned within the BepiColombo mission (Benkhoff
341 et al., 2010). An almost identical instrument to CENA (Saito et al., 2010)
342 and another ENA imager at high angular resolution, ELENA (Orsini et al.,
343 2010), will be used for recording the ENA images. Unlike the Moon, Mercury
344 has a dipole magnetic field, which, under nominal conditions, shields a large
345 fraction of the Hermean surface from the solar wind. The open field line
346 in the cusp region, though, allow solar wind protons to precipitate onto
347 the surface (e.g. Kallio and Janhunen (2003)). Imaging of these regions in
348 backscattered hydrogen would reveal the open / closed field line boundary,
349 particle precipitation pattern, and magnetospheric dynamics.

6. Acknowledgments

P. Wurz gratefully acknowledges financial support by the Swiss National Science Foundation.

Captions

Figure 1: ENA maps with focus on the the South Pole - Aitken basin. The two different ENA reflection ratio maps depict the reflection ratios in the low energy range (panel a) and in the high energy range (panel b) separately. Also shown is the effective exposure time (see text for details; panel c) and the map showing the magnetic field at 30 km altitude as measured by Lunar Prospector (panel d). The approximate extension of the ENA feature is described by the red polygon, whereas the ellipse fitting the topography data best is over-plotted in white.

Figure 2: Maps of the five major features in the South Pole Aitken Basin area. Panel a) depicts Clementine laser altimeter data, panels b) and c) display Lunar Prospector gamma-ray spectrometer iron and thorium data, panel d) depicts a global Clementine 750 nm spectral reflectance mosaic, and panel e) shows the magnetic field at 30 km altitude as measured by Lunar Prospector. In addition, panel f) shows five regions of interest: region 1 depicts the area where the ENA feature and the magnetic feature extend beyond the topography feature, regions 2 and 5 depict the areas where the ENA feature and the magnetic field feature coincide with the topography feature, region 3 depicts the area where the topography feature is strong,

but not the iron, thorium or albedo feature, and region 4 depicts the area where the topography and the albedo feature are strong, but not the iron or the thorium feature. In all panels, the white (gray) ellipse shows the best fit to the topography data, the red polygon describes the approximate extension of the ENA feature, and in panels b) and c) the yellow ellipses show the best fits to the respective chemical data.

Table 1: Surface projections of the central five sectors given in lunar longitude/latitude as well as kilometers for two nominal spacecraft altitudes (100 km and 200 km).

Table 2: Averages of the major features for the five different regions depicted in Figure 2 panel f). The values are denoted with low, medium, and high according to the following ranges. Elevation: $[-8...-2.5, -2.5...2.5, 2.5...8]$, visible albedo: $[<70, 70...140, >140]$, magnetic field: $[<1.5, 1.5...3, >3]$, iron: $[<7, 7...9, >9]$, thorium: $[<2, 2...3, >3]$, ENAs: $[<15, 15...17, >17]$.

Table 3: Linear Pearson correlation coefficients computed from the mean values presented in Table 2 for the ENA maps and the other features.

Bibliography

- Barabash, S., Bhardwaj, A., Wieser, M., Sridharan, R., Kurian, T., Varier, S., Vijayakumar, E., Abhirami, V., Raghavendra, K.V., Mohankumar, S.V., Dhanya, M.B., Thampi, S., Kazushi, A., Andersson, H., Yoshifumi, F., Holmström, M., Lundin, R., Svensson, J., Karlsson, S., Piazza, D., Wurz, P., 2009. Investigation of the solar wind-Moon interaction onboard Chandrayaan-1 mission with the SARA experiment. *Curr. Sci.* 96, 526–532.
- Benkhoff, J., van Casteren, J., Hayakawa, H., Fujimoto, M., Laakso, H., Novara, M., Ferri, P., Middleton, H.R., Ziethe, R., 2010. BepiColombo - Comprehensive exploration of Mercury: Mission overview and science goals. *Planet. Space Sci.* 58, 2–20.
- Bhardwaj, A., Barabash, S., Futaana, Y., Kazama, Y., Asamura, K., Sridharan, R., Holmström, M., Wurz, P., Lundin, R., 2005. Low energy neutral atom imaging on the Moon with the SARA instrument aboard Chandrayaan-1 mission. *Journal of Earth System Sciences* 114, 749–760.
- Crider, D., Vondrak, R., 2002. Hydrogen migration to the lunar poles by solar wind bombardment of the Moon. *Adv. Space Res.* 30, 1869–1874.

- Feldman, W., Lawrence, D., Elphic, R., Barraclough, B., Maurice, S., Genetay, I., Binder, A., 2000. Polar hydrogen deposits on the Moon. *J. Geophys. Res.* 105, 4175–4176.
- Futaana, Y., Barabash, S., Wieser, M., Lue, C., Wurz, P., Vorburger, A., Bhardwaj, A., Asamura, K., 2013. Remote energetic neutral atom imaging of electric potential over a lunar magnetic anomaly. *Geophys. Res. Lett.* 40, 262–266.
- Futaana, Y., Machida, S., Saito, Y., Matsuoka, A., Hayakawa, H., 2003. Moon-related nonthermal ions observed by Nozomi: Species, sources and generation mechanism. *J. Geophys. Res.* 108, 1025.
- Garrick-Bethell, I., Zuber, M.T., 2009. Elliptical structure of the lunar South Pole-Aitken basin. *Icarus* 204, 399–408.
- Goswami, J., Annadurai, M., 2009. Chandrayaan-1: India’s first planetary science mission to the Moon. *Curr. Sci.* 96, 486–491.
- Halekas, J.S., Poppe, A.R., McFadden, J.P., Glassmeier, K.H., 2013. The effects of reflected protons on the plasma environment of the moon for parallel interplanetary magnetic fields. *Geophys. Res. Lett.* 40, 4544–4548.

- Hood, L.L., Richmond, N.C., Spudis, P.D., 2013. Origin of strong lunar magnetic anomalies: Further mapping and examinations of LROC imagery in regions antipodal to young large impact basins. *J. Geophys. Res.* 118, 1265–1284.
- Kallio, E., Janhunen, P., 2003. Solar wind and magnetospheric ion impact on Mercury’s surface. *Geophys. Res. Lett.* 30, 1877.
- Kazama, Y., Barabash, S., Wieser, M., Asamura, K., Wurz, P., 2007. Development of an LENA instrument for planetary missions by numerical simulations. *Planet. Space Sci.* 55, 1518–1529.
- Lawrence, D.J., Feldman, W.C., Barraclough, B.L., Binder, A.B., Elphic, R.C., Maurice, S., Thomsen, D.R., 1998. Global Elemental Maps of the Moon: The Lunar Prospector Gamma-Ray Spectrometer. *Science* 281, 1484.
- Lawrence, D.J., Feldman, W.C., Elphic, R.C., Little, R.C., Prettyman, T.H., Maurice, S., Lucey, P.G., Binder, A.B., 2002. Iron abundances on the lunar surface as measured by the Lunar Prospector gamma-ray and neutron spectrometers. *J. Geophys. Res.* 107, 5130.
- Lee, E.M., Gaddis, L.R., Weller, L., Richie, J.O., Becker, T., Shinaman, J.,

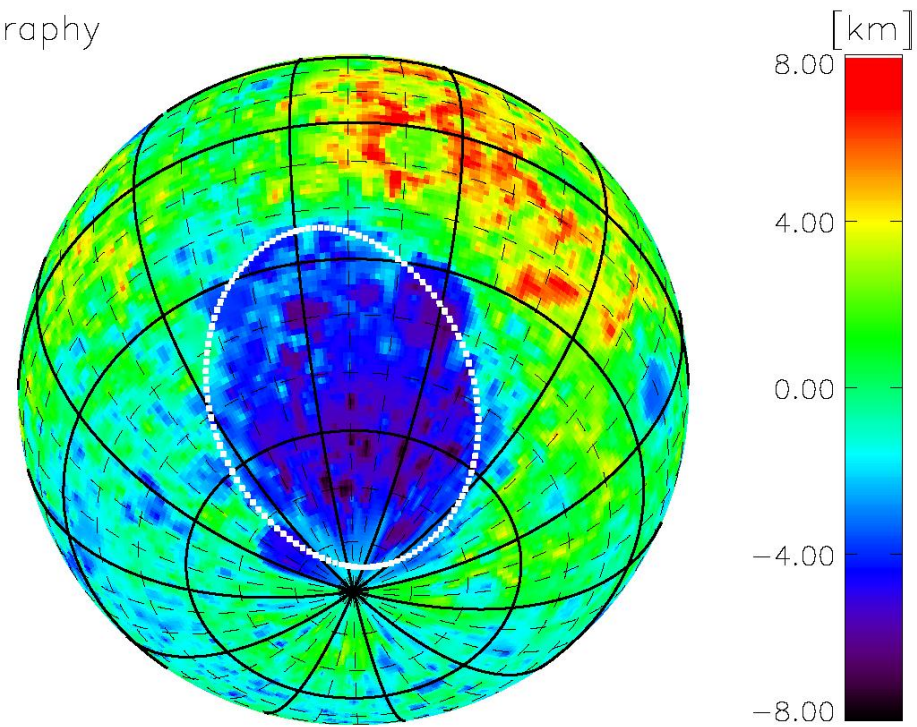
- Rosiek, M.R., Archinal, B.A., 2009. A New Clementine Basemap of the Moon, in: Lunar and Planetary Science Conference, p. 2445.
- Lin, R., Mitchell, D., Curtis, D., Anderson, K., Carlson, C., McFadden, J., Acuña, M., Hood, L., Binder, A., 1998. Lunar surface magnetic fields and their interaction with the solar wind: Results from Lunar Prospector. *Planet. Space Sci.* 281, 1480–1484.
- Lue, C., Futaana, Y., Barabash, S., Wieser, M., Holmström, M., Bhardwaj, A., Dhanya, M.B., Wurz, P., 2011. Strong influence of lunar crustal fields on the solar wind flow. *Geophys. Res. Lett.* 38, 3202.
- McComas, D., Allegrini, F., Bochsler, P., Frisch, P., Funsten, H., Gruntman, M., Janzen, P., Kucharek, H., Möbius, E., Reisenfeld, D., Schwadron, N., 2009. Lunar backscatter and neutralization of the solar wind: First observations of neutral atoms from the Moon. *Geophys. Res. Lett.* 36, 12104.
- McFadden, L.A.A., Weissman, P.R., Johnson, T.V., 2007. Encyclopedia of the solar system. Academic Press, San Diego, CA, USA.
- Mitchell, D., Halekas, J., Lina, R., Freya, S., Hood, L., Acuña, M., Binder,

- A., 2008. Global mapping of lunar crustal magnetic fields by lunar prospector. *Icarus* 194, 401–409.
- Niehus, H., Heiland, W., Taglauer, E., 1993. Low-energy ion scattering at surfaces. *Surf. Sci. Rep.* 17, 213–303.
- Orsini, S., Livi, S., Torkar, K., Barabash, S., Milillo, A., Wurz, P., di Lellis, A.M., Kallio, E., The Serena Team, 2010. SERENA: A suite of four instruments (ELENA, STROFIO, PICAM and MIPA) on board BepiColombo-MPO for particle detection in the Hermean environment. *Planet. Space Sci.* 58, 166–181.
- Purucker, M.E., Sabaka, T.J., Halekas, J., Olsen, N., Tsyganenko, N., Hood, L.L., 2006. The Lunar Magnetic Field Environment: Interpretation of New Maps of the Internal and External Fields, in: Mackwell, S., Stansbery, E. (Eds.), 37th Annual Lunar and Planetary Science Conference, p. 1933.
- Richmond, N., Hood, L., 2008. A preliminary global map of the vector lunar crustal magnetic field based on Lunar Prospector magnetometer data. *J. Geophys. Res.* 113, 2010.
- Saito, Y., Sauvaud, J.A., Hirahara, M., Barabash, S., Delcourt, D., Takashima, T., Asamura, K., BepiColombo MMO/MPPE Team, 2010.

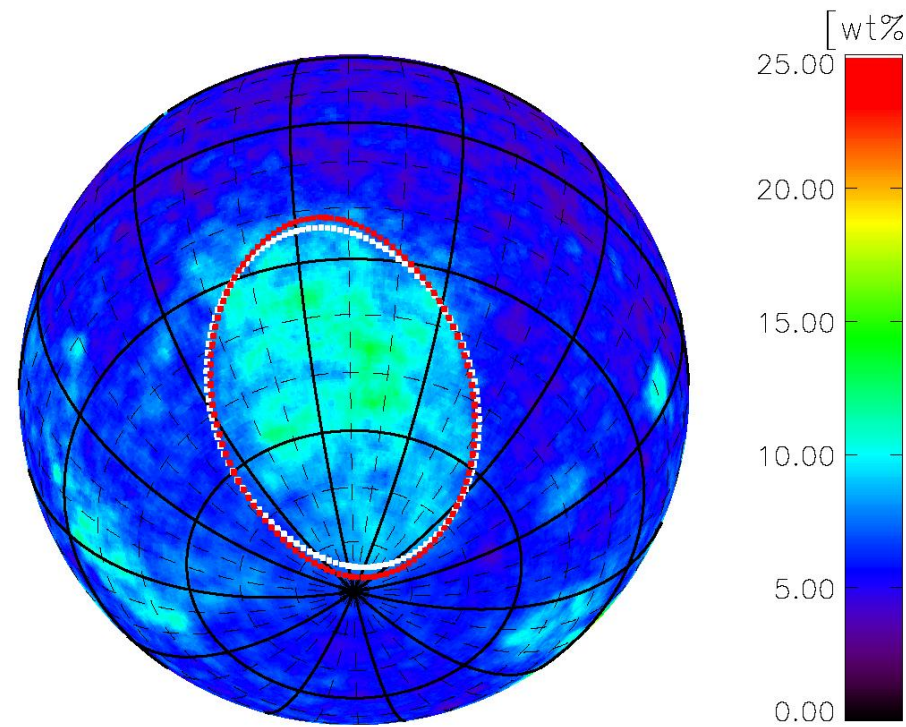
- Scientific objectives and instrumentation of Mercury Plasma Particle Experiment (MPPE) onboard MMO. *Planet. Space Sci.* 58, 182–200.
- Saito, Y., Yokota, S., Tanaka, T., Asamura, K., Nishino, M.N., Fujimoto, M., Tsunakawa, H., Shibuya, H., Matsushima, M., Shimizu, H., Takahashi, F., Mukai, T., Terasawa, T., 2008. Solar wind proton reflection at the lunar surface: Low energy ion measurement by MAP-PACE onboard SELENE (KAGUYA). *Geophys. Res. Lett.* 35, 24205.
- Vorburger, A., Wurz, P., Barabash, S., Wieser, M., Futaana, Y., Holmström, M., Bhardwaj, Asamura, K., 2012. Energetic neutral atom observations of magnetic anomalies on the lunar surface. *J. Geophys. Res.* 117, 7208.
- Vorburger, A., Wurz, P., Barabash, S., Wieser, M., Futaana, Y., Holmström, M., Bhardwaj, A., Asamura, K., 2014. First direct observation of sputtered lunar oxygen. *Journal of Geophysical Research (Space Physics)* 119, 709–722.
- Vorburger, A., Wurz, P., Barabash, S., Wieser, M., Futaana, Y., Lue, C., Holmström, M., Bhardwaj, A., Dhanya, M.B., Asamura, K., 2013. Energetic neutral atom imaging of the lunar surface. *J. Geophys. Res.* 118, 3937–3945.

- Wang, X.D., Bian, W., Wang, J.S., Liu, J.J., Zou, Y.L., Zhang, H.B., Lü, C., Liu, J.Z., Zuo, W., Su, Y., Wen, W.B., Wang, M., Ouyang, Z.Y., Li, C.L., 2010. Acceleration of scattered solar wind protons at the polar terminator of the Moon: Results from Chang'E-1/SWIDs. *Geophys. Res. Lett.* 37, 7203.
- Wieczorek, M.A., Weiss, B.P., Stewart, S.T., . An Impactor Origin for Lunar Magnetic Anomalies. *Science* 335, 1212–1215.
- Wieser, M., Barabash, S., Futaana, Y., Holmström, M., Bhardwaj, A., Sridharan, R., Dhanya, M., Schaufelberger, A., Wurz, P., Asamura, K., 2010. First observation of a minimagnetosphere above a lunar magnetic anomaly using energetic neutral atoms. *Geophys. Res. Lett.* 37, 5103.
- Wieser, M., Barabash, S., Futaana, Y., Holmström, M., Bhardwaj, A., Sridharan, R., Dhanya, M., Wurz, P., Schaufelberger, A., Asamura, K., 2009. Extremely high reflection of solar wind protons as neutral hydrogen atoms from regolith in space. *Planet. Space Sci.* 57, 2132–2134.
- Zhang, W., Bowles, N.E., 2013. Mapping lunar TiO_2 and FeO with M3 data. *European Planetary Science Congress 2013* 8, 374.

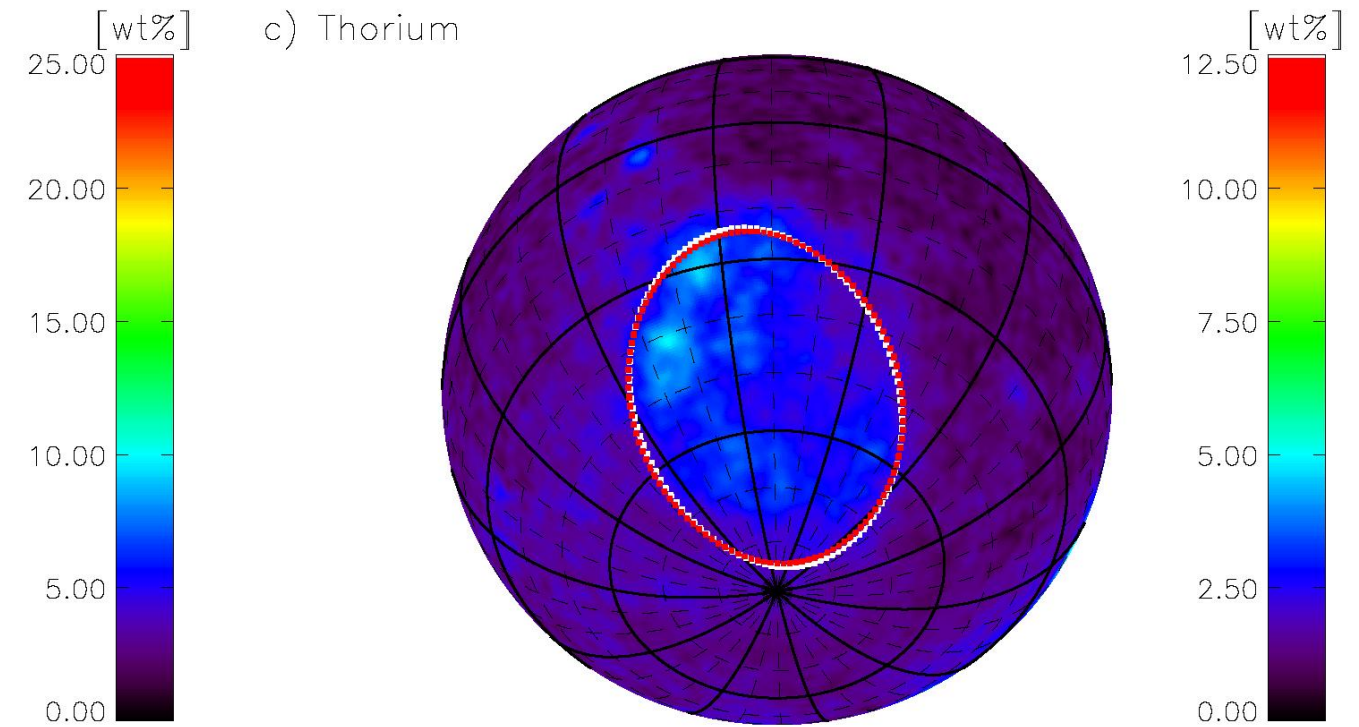
a) Topography



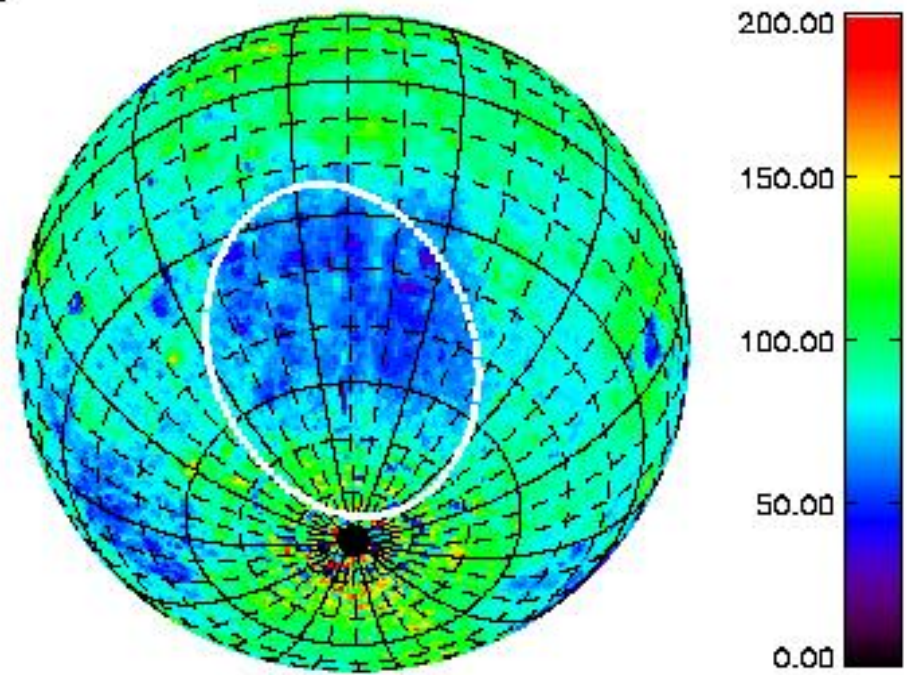
b) Iron



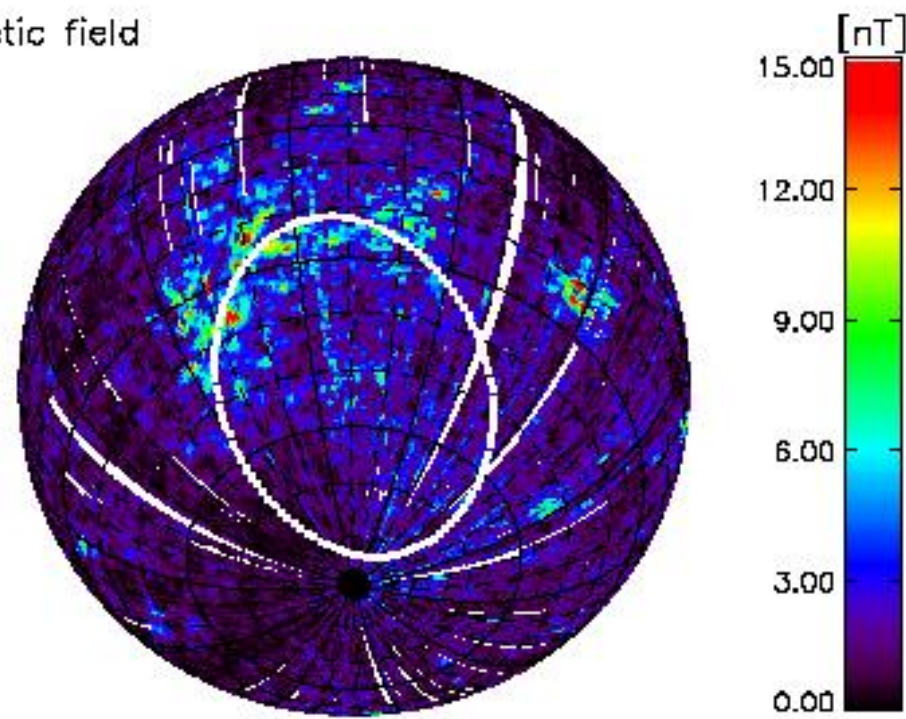
c) Thorium



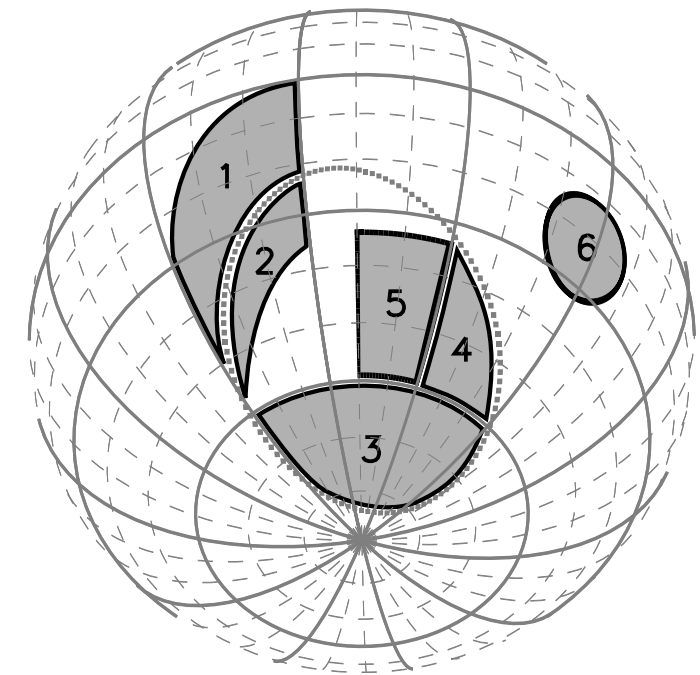
d) Albedo



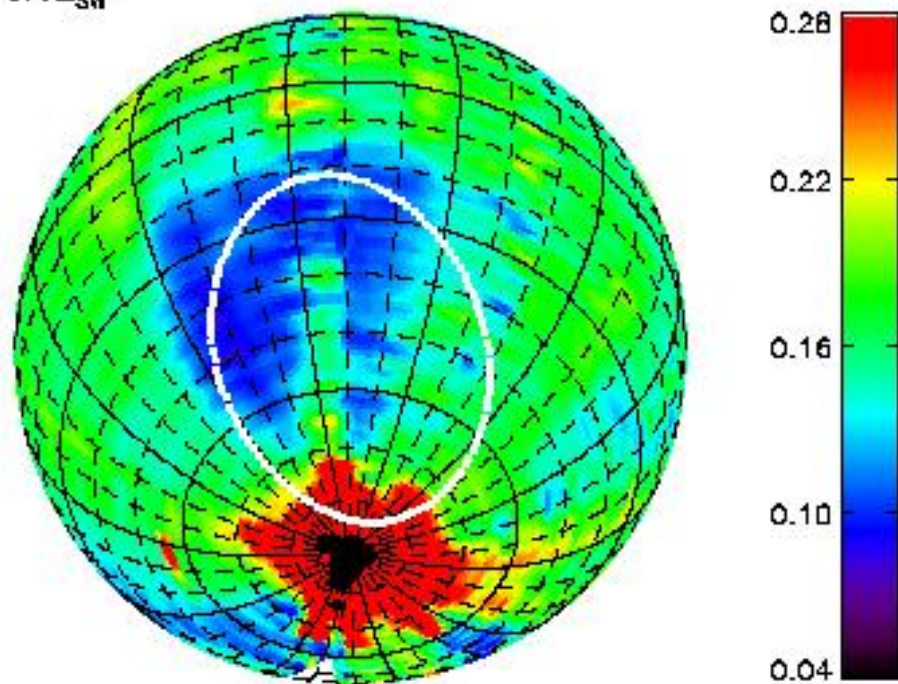
e) Magnetic field



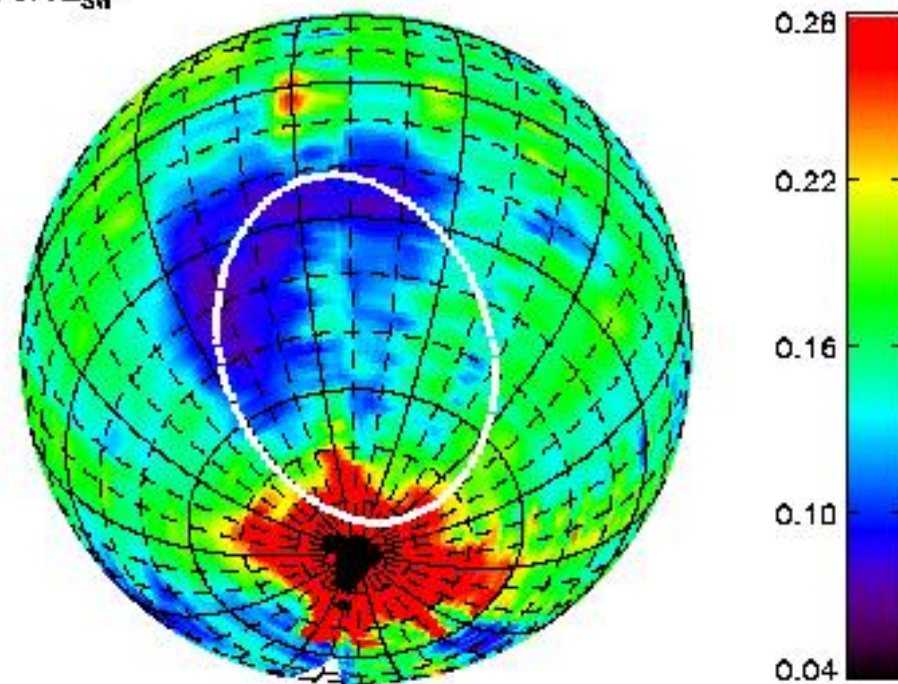
f) Regions of interest



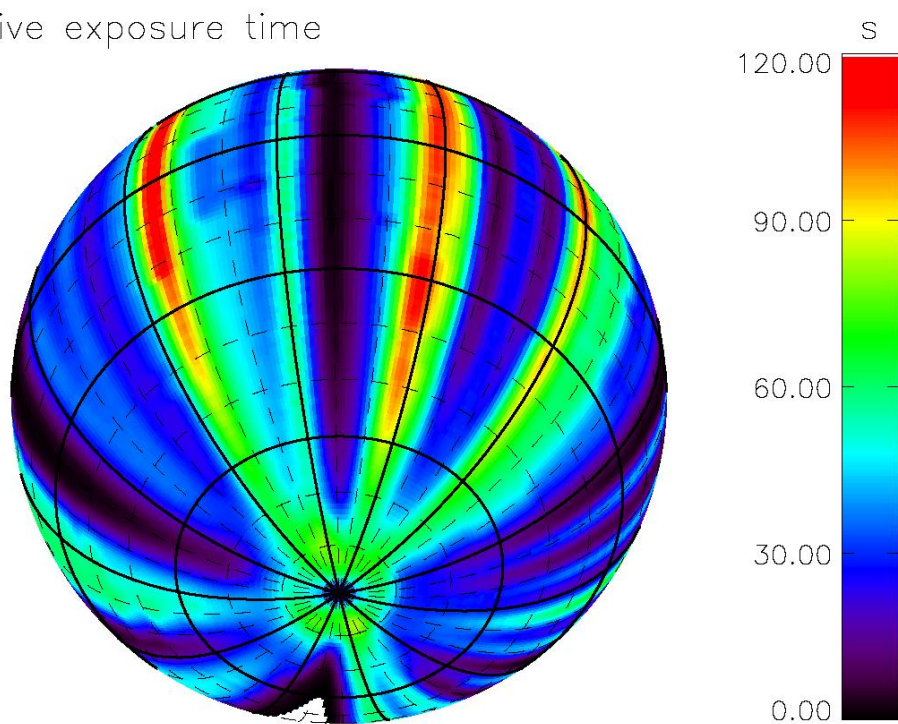
a) $E < 30\%E_{SW}$



b) $E > 30\%E_{SW}$



c) Effective exposure time



d) Magnetic field

